From Fe3O4/NiO bilayers to NiFe2O4-like thin films through Ni interdiffusion

Kuschel, O.; Buss, R.; Spiess, W.; Schemme, T.; Woellermann, J.; Balinski, K.; N'Diaye, A. T.; Kuschel, T.; Wollschlaeger, J.; Kuepper, K.

Published in:
Physical Review B

DOI:
10.1103/PhysRevB.94.094423

Publication date:
2016

From Fe_3O_4/NiO bilayers to $NiFe_2O_4$-like thin films through Ni interdiffusion

O. Kuschel,[1] R. Buß,[1] W. Spiess,[1] T. Schemme,[1] J. Wöllermann,[1] K. Balinski,[1] A. T. N'Diaye,[2] T. Kuschel,[3,4] J. Wollschläger,[1,5,*] and K. Kuepper[1,5,†]

[1]*Department of Physics, Barbarastraße 7, Osnabrück University, 49076 Osnabrück, Germany*

[2]*Advanced Light Source, Lawrence Berkeley National Laboratory, California 94720, USA*

[3]*Center for Spinelectronic Materials and Devices, Department of Physics, Bielefeld University, 33615 Bielefeld, Germany*

[4]*Physics of Nanodevices, Zernike Institue for Advanced Materials, University of Groningen, 9747 AG Groningen, Netherlands*

[5]*Center of Physics and Chemistry of New Materials, Osnabrück University, 49076 Osnabrück, Germany*

(Received 9 February 2016; revised manuscript received 1 July 2016; published 20 September 2016)

Ferrites with (inverse) spinel structure display a large variety of electronic and magnetic properties, making some of them interesting for potential applications in spintronics. We investigate the thermally induced interdiffusion of Ni^{2+} ions out of NiO into Fe_3O_4 ultrathin films, resulting in off-stoichiometric nickel ferrite–like thin layers. We synthesized epitaxial Fe_3O_4/NiO bilayers on Nb-doped $SrTiO_3$(001) substrates by means of reactive molecular beam epitaxy. Subsequently, we performed an annealing cycle comprising three steps at temperatures of 400 °C, 600 °C, and 800 °C under an oxygen background atmosphere. We studied the changes of the chemical and electronic properties as result of each annealing step with help of hard x-ray photoelectron spectroscopy and found a rather homogeneous distribution of Ni and Fe cations throughout the entire film after the overall annealing cycle. For one sample we observed a cationic distribution close to that of the spinel ferrite $NiFe_2O_4$. Further evidence comes from low-energy electron diffraction patterns indicating a spinel-type structure at the surface after annealing. Site- and element-specific hysteresis loops performed by x-ray magnetic circular dichroism uncovered the antiferrimagnetic alignment between the octahedral coordinated Ni^{2+} and Fe^{3+} ions and the Fe^{3+} ion in tetrahedral coordination. We find a quite low coercive field of 0.02 T, indicating a rather low defect concentration within the thin ferrite films.

DOI: 10.1103/PhysRevB.94.094423

I. INTRODUCTION

Iron oxides are of special interest due to a number of astonishing properties dependent on the Fe valence state and the underlying crystallographic and electronic structure. Magnetite (Fe_3O_4) is among the most studied ferrites due to its ferrimagnetic ordered ground state with a saturation moment of $4.07\mu_B$ per formula unit and a high Curie temperature of 860 K for bulk material [1,2]. This magnetic ground state is accompanied by half metallicity; that is, only one spin orientation is present at the Fermi energy [3], making this material a potential candidate for future spintronic devices with 100% spin polarization [4,5]. Magnetite crystallizes in the cubic inverse spinel structure (equal distribution of Fe^{3+} on A and B sites and Fe^{2+} exclusively on B sites) with lattice constant $a = 0.8396$ nm (space group $Fd3m$). The oxygen anions form an fcc anion sublattice.

Often, Fe_3O_4 thin films are grown on cubic MgO(001) substrates by various deposition techniques [6–11] since the lattice mismatch between Fe_3O_4 and MgO(001) ($a = 0.42117$ nm) is only 0.3%, comparing the oxygen sublattices. A severe limit of epitaxial thin-film growth on MgO substrates is Mg^{2+} segregation into the Fe_3O_4 film if the substrate temperature is above 250 °C [12]. Mg-rich interfaces [13] and Mg interdiffusion have been studied in detail [14], having significant influence on interface roughness or antiphase boundaries. Thus, the underlying electronic and magnetic structure influences the properties of the magnetite thin film in question or the tunnel magnetoresistance in magnetic tunnel junctions with magnetite electrodes [15–18].

A potential approach to minimize or suppress Mg segregation, besides rather low substrate temperatures during magnetite growth, is an additional buffer layer, e.g., metallic iron [19] or NiO [20] between Fe_3O_4 and the substrate. This approach is also of interest with respect to the possibility of building a full oxidic spin valve making use of the exchange bias between the ferrimagnetic magnetite and the antiferromagnetic nickel oxide [20–22].

The usage of other substrates like $SrTiO_3$ could also prevent Mg interdiffusion. Despite the large lattice mismatch of −7.5% between the doubled $SrTiO_3$ bulk lattice constant (0.3905 nm) and magnetite, it is possible to grow epitaxial Fe_3O_4 films on the $SrTiO_3$(001) surface [23,24]. In particular, concerning coupled Fe_3O_4/NiO bilayers grown on $SrTiO_3$, so far only Pilard *et al.* have reported on the magnetic properties of the Fe_3O_4/NiO interface [25]. On the other hand, $NiFe_2O_4$ thin films are of huge interest nowadays since they are magnetic insulators or semiconductors. Therefore, they can be used as spin filters [26] or for thermal induction of spin currents via the spin Seebeck effect [27,28]. Furthermore, electrical charge transport and spin currents can be manipulated by the spin Hall magnetoresistance using $NiFe_2O_4$ thin films adjacent to nonmagnetic material [29].

Therefore, we study here the possibility to form nickel ferrite starting with a distinct Fe_3O_4/NiO bilayer grown on Nb-doped $SrTiO_3$(001). Knowledge about the modification of the underlying crystallographic, electronic, and magnetic structure by Ni interdiffusion is indispensable for potential applications. We also want to investigate fundamental aspects, especially of Ni^{2+} diffusion from a NiO buffer layer into a Fe_3O_4 top layer as well as NiO surface segregation through

*jwollsch@uos.de
†kkuepper@uos.de

the Fe_3O_4 film, since knowledge of diffusion processes in oxides still appears to be quite rudimentary for many systems.

We perform a systematic three-step annealing cycle of Fe_3O_4/NiO bilayers after synthesis and simultaneously investigating surface crystallographic and "bulk" electronic structure changes by means of low energy electron diffraction (LEED) and hard x-ray photoelectron spectroscopy (HAXPES). Furthermore, we carry out structural analysis before and after the overall annealing cycle employing x-ray reflectivity (XRR) and synchrotron-radiation-based x-ray diffraction (SR-XRD), as well as element- and site-specific x-ray magnetic circular dichroism (XMCD) after the overall annealing cycle to analyze the resulting magnetic properties in detail.

II. EXPERIMENTAL DETAILS

Two samples with ultrathin Fe_3O_4/NiO bilayers on conductive 0.05 wt% Nb-doped $SrTiO_3(001)$ substrates have been prepared using the technique of reactive molecular beam epitaxy (RMBE). The substrates have been supplied with a polished surface and were annealed once at 400 °C for 1 h in an oxygen atmosphere of 1×10^{-4} mbar prior to deposition. Afterwards, the chemical cleanness and composition was proven by XPS, while the crystallinity of the surface was checked by LEED. Oxide films have been deposited by thermal evaporation from pure metal rods in low oxygen atmosphere. During film growth, the substrate was heated to 250 °C, while the oxygen pressure was kept at 1×10^{-5} mbar for NiO and 5×10^{-6} mbar for Fe_3O_4 to guarantee optimal oxidation condition. Deposition rates of 0.85 and 4.6 nm/min were used for the growth of NiO and Fe_3O_4 films, respectively, which was controlled by a quartz microbalance adjacent to the source. One sample was created with a 5.6-nm NiO film (sample A), and the other was created with a 1.5-nm NiO film (sample B). Thereafter, 5.5-nm-thick Fe_3O_4 films were deposited on the NiO films. Film stoichiometry and surface structure have been monitored *in situ* by x-ray photoelectron spectroscopy (XPS) using Al K_α radiation and LEED, respectively.

The samples were transported under ambient conditions to the Diamond Light Source (DLS) synchrotron, where the effects of annealing on the bilayer system were studied at beamline I09 by heating the samples in three steps at 400 °C, 600 °C, and 800 °C for 20 to 30 min in an oxygen atmosphere of 5×10^{-6} mbar to avoid reduction or further oxidation of the sample [30]. Prior to and after the annealing studies XRR measurements at 2.5 keV photon energy were performed to determine the film thickness. After each annealing step, the films were studied *in situ* by soft x-ray photoemission and HAXPES to clarify the chemical composition in the near-surface region and in the bulk region, respectively. In addition, LEED measurements were performed to check the crystallinity of the individual layers of the NiO/Fe_3O_4 bilayer.

For HAXPES an energy of $h\nu = 5934$ eV was used, creating photoelectrons with high kinetic energy, which allows a higher probing depth compared to soft x-ray photoemission ($h\nu = 1000$ eV).

The information depth D_I, from which 95% of the photoelectrons originate, is defined as

$$D_I(95) = -\lambda\cos\varphi\ln(1-95/100), \quad (1)$$

with the inelastic mean free path λ and the off-normal emission angle φ [31]. The maximum information depth for the Fe $2p$ core level for HAXPES and soft x-ray photoemission measurements is 22 and 2.5 nm, respectively, estimating λ with the Tanuma Powell and Penn algorithm (TPP-2M) formula [32]. As the beamline features a two-dimensional photoelectron detector, which can be operated in an angular mode, photoelectron spectra at different emission angles were acquired, each with an acceptance angle of $\sim7°$.

Subsequently, structural analysis of the annealed films was performed using SR-XRD, while the resulting film thickness and layer structure of these films were determined by means of laboratory-based XRR using Cu K_α radiation. SR-XRD experiments have been carried out *ex situ* at PETRA III beamline P08 (DESY, Germany) using a photon energy of 15 keV. In both cases the measurements were performed in θ-2θ diffraction geometry. For the analysis of all XRR experiments an in-house-developed fitting tool based on the Parratt algorithm [33] and Névot-Croce roughness model [34] was used. The SR-XRD measurements were analyzed by calculating the crystal truncation rod (CTR) intensity within the full kinematic diffraction theory to fit the experimental diffraction data.

XMCD spectroscopy was performed at the Fe $L_{2,3}$ and Ni $L_{2,3}$ edges with the samples at room temperature at beamline 6.3.1 of the Advanced Light Source, Lawrence Berkeley Laboratory. We utilized total electron yield (TEY) as the detection mode. The external magnetic field of 1.5 T was aligned parallel to the x-ray beam and was switched for each energy. The angle between the sample surface and x-ray beam was chosen to be 30°. The resolving power of the beamline was set to $E/\Delta E \sim 2000$; the degree of circular polarization was about 55%. For the analysis of the Fe $L_{2,3}$ XMCD spectra, we performed corresponding model calculations within the atomic multiplet and crystal-field theory including charge transfer using the program CTM4XAS [35,36].

III. RESULTS

A. Surface characterization

In Figs. 1(a)–1(c) the LEED patterns of the cleaned substrate and the as-prepared NiO and Fe_3O_4 films are presented for sample A. Figures 1(d) and 1(e) show the LEED images recorded after the last annealing step of 800 °C for sample A and sample B, respectively.

After cleaning of the $SrTiO_3$ substrates the LEED pattern shows very sharp diffraction spots of a (1×1) surface with square structure and negligible background intensity [see Fig. 1(a)], indicating a clean (001)-oriented surface with long-range structural order. Additionally, XPS measurements show chemically clean substrates without carbon contamination (not shown here).

The LEED image recorded directly after RMBE of NiO also exhibits a quadratic (1×1) structure [see Fig. 1(b)], as expected for the NiO(001) surface unit cell. However, the pattern is rotated by 45° and is $\sim\sqrt{2}$ times larger than the pattern of the $SrTiO_3(001)$ substrate. The broadening of the diffraction spots is most likely caused by defects due

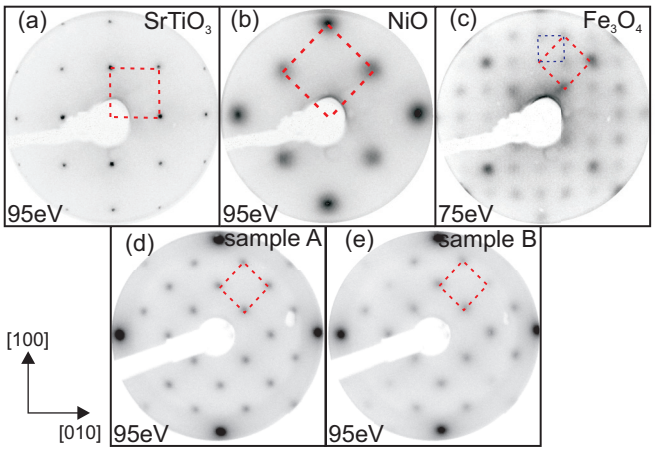

FIG. 1. LEED patterns for sample A recorded directly after (a) preparation of the $SrTiO_3$ substrate, (b) deposition of NiO, (c) deposition of Fe_3O_4, and (d) the last annealing step of 800 °C. For comparison, (e) shows the LEED pattern for sample B after the final annealing step. Marked with red squares are the respective (1×1) surface unit cells in reciprocal space. The blue square indicates the $(\sqrt{2}\times\sqrt{2})$R45° superstructure typical for magnetite.

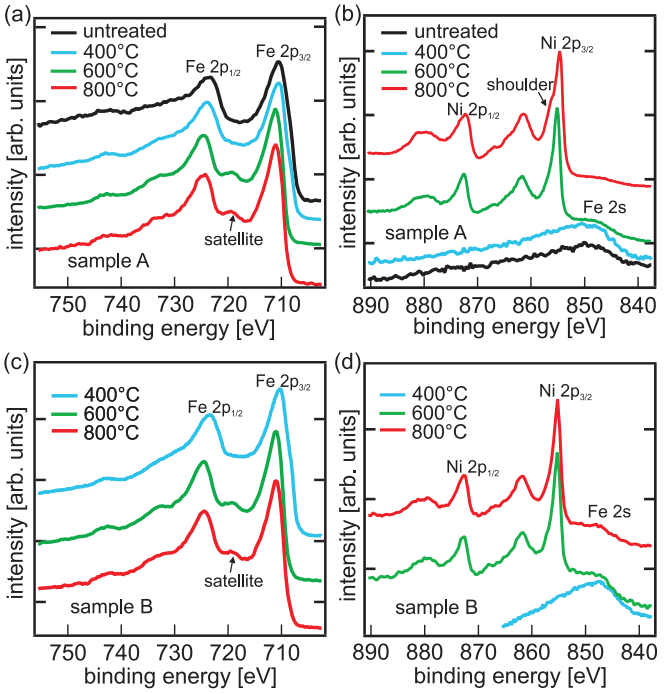

FIG. 2. Soft XPS spectra of (a) Fe 2p and (b) Ni 2p regions of sample A and (c) Fe 2p and (d) Ni 2p regions of sample B after each annealing step. For sample A the spectra of the untreated sample are shown exemplarily.

to relaxation processes induced by the high lattice misfit of −6.9% for NiO(001) compared to $SrTiO_3$(001).

The LEED pattern of the as-prepared Fe_3O_4 film [see Fig. 1(c)] reveals a quadratic (1×1) surface structure with almost doubled periodicity compared to NiO as the real-space lattice constant of the magnetite inverse spinel structure is about twice as large, giving a lattice misfit of only 0.5% for Fe_3O_4(001) on NiO(001). Furthermore, additional diffraction spots of a $(\sqrt{2}\times\sqrt{2})$R45° superstructure can be seen, which is characteristic of well-ordered Fe_3O_4(001) surfaces [37–39].

LEED results indicate a cube-on-cube growth for both NiO and Fe_3O_4 films. Additionally, the Ni 2p and Fe 2p XPS spectra recorded directly after preparation of each film (not shown here) exhibit a characteristic shape for Ni^{2+} and mixed Fe^{2+}/Fe^{3+} valence states, respectively. Thus, combining the results from XPS and LEED, we can conclude that the as-prepared films consist of stoichiometric Fe_3O_4/NiO bilayers.

Figure 2 shows the Fe 2p and Ni 2p core-level spectra of both samples after transport to DLS under ambient conditions (sample A) and after each annealing step using soft XPS.

After the first annealing step at 400 °C, the Fe 2p peak shape is similar to that of the untreated sample [see Fig. 2(a)]. No charge-transfer satellites are visible, indicating Fe_3O_4 stoichiometry and the presence of a mixed oxidation state [40,41]. For both samples, Fe 2$p_{3/2}$ and Fe 2$p_{1/2}$ peaks are located at binding energies of 710.4 (±0.2) and 723.8 (±0.2) eV, respectively, corresponding to the values for magnetite known from the literature [40]. Furthermore, no Ni 2p signal is visible for both samples due to the small information depth, demonstrating that Ni did not diffuse into the Fe_3O_4 film and that the Fe_3O_4 film was not deconstructed [see Figs. 2(b) and 2(d)]. Consequently, the first annealing step at 400 °C only removed surface contaminations from the transport, without effecting the initial layer structure of the sample.

After the annealing step at 600 °C, a distinctive satellite typical for trivalent iron becomes visible between the Fe 2$p_{1/2}$ and Fe 2$p_{3/2}$ peaks for sample A and sample B [see Figs. 2(a) and 2(c)]. Further, Fe 2$p_{1/2}$ and Fe 2$p_{3/2}$ are shifted to binding energies of 710.9 (±0.2) and 724.4 (±0.2) eV, respectively. The shift to higher binding energies and the satellite at ∼8 eV above the main peak confirm the presence of Fe^{3+} and a deficiency of divalent iron [40–42].

In contrast to lower annealing temperature, Ni 2p peaks becomes visible after the 600 °C annealing step. Both samples show an intense Ni 2p signal consisting of two main peaks accompanied by satellite peaks at ∼7 eV above their binding energies. The shape of the spectra and, in particular, the absence of a shoulder on the high-energy side of Ni 2$p_{3/2}$ indicate that no NiO cluster has been formed at the surface of both samples [43,44]. The occurrence of such a shoulder ∼1.5 eV above the 2$p_{3/2}$ peak is reported to be characteristic of NiO [45,46]. The binding energy of 855.2 (±0.2) eV of the Ni 2$p_{3/2}$ peak also confirms the origin of $NiFe_2O_4$ and not of NiO [43,47]. Thus, both iron and nickel spectra obtained after annealing at 600 °C point to the formation of $NiFe_2O_4$ at the near-surface region of both samples as a result of intermixing.

The last annealing step at 800 °C influences the peak shape of neither the Fe 2p nor the Ni 2p spectra of sample B [see Figs. 2(c) and 2(d)], indicating a complete intermixing of the two layers already after the annealing at 600 °C. However, for sample A a NiO-specific shoulder on the high-energy side of Ni 2$p_{3/2}$ appears [see Fig. 2(b)]. Further, a shift to lower binding energies takes place, resulting in a binding energy of 854.5 (±0.2) eV for Ni 2$p_{3/2}$, indicating the presence of NiO at the surface [43]. Since there is no change in the Fe 2p spectra for sample A, we conclude that NiO clusters are formed at the surface of a $NiFe_2O_4$-like film.

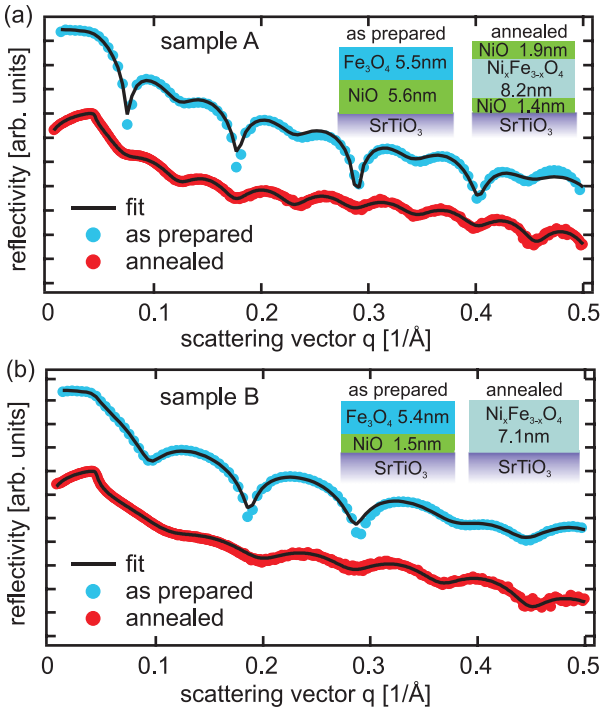

FIG. 3. Reflectivity curves and calculations from XRR measurements before and after the annealing experiments (a) for sample A and (b) for sample B. The insets show the underlying models.

LEED patterns of samples A and B recorded after the final annealing step are presented in Figs. 1(d) and 1(e). The diffraction pattern can be attributed to the (001)-(1×1) surface of nickel ferrite, which shows a lattice constant similar to that of magnetite [see Fig. 1(c)]. However, the $(\sqrt{2}\times\sqrt{2})$R45° superstructure indicative of magnetite is not observed after the final annealing step. Therefore, this result underpins the formation of nickel ferrite, as concluded before from XPS where Fe^{3+} is primarily observed. Furthermore, the LEED spots of sample A are sharper than the spots of sample B. We attribute this finding to the formation of a stoichiometric $NiFe_2O_4$ film for sample A, while the ferrite film is less ordered for sample B, in which the Ni content of the film is too low (see below). The formation of NiO islands concluded from our detailed XRR analysis cannot clearly be concluded from the LEED experiments since the diffraction peaks of the NiO film coincide with diffraction peaks from the nickel ferrite film due to the coincidence between the nickel ferrite lattice constant and the doubled NiO lattice constant.

B. XRR

Figure 3 shows the measured and calculated XRR intensities obtained at DLS prior to the annealing experiments for both samples. The XRR intensity obtained from sample A clearly shows the beating of two layers with almost identical thickness, while the intensity obtained from sample B points to two layers with very different thickness. In addition, the data show well-defined intensity oscillations for both samples, pointing to a double-layer structure and flat homogeneous interfaces and films. For the calculation of the intensity distributions and the exact layer structure a basic model was used, consisting of a magnetite film on top of a NiO layer on a $SrTiO_3$ substrate (insets of Fig. 3). In Table I the fit parameters, e.g., dispersion δ and rms roughness σ, are shown. Here, the obtained values for the dispersion of the as-prepared samples are within 1% of corresponding literature values [48].

The measured and calculated XRR intensities of the annealed samples as well as the model used are also presented in Fig. 3. For both samples the XRR shows clear intensity oscillations with a changed periodicity compared to the as-prepared films. Taking into account the electron densities and layer structures obtained from XRR, this effect can be attributed to an intermixing of the two initial oxide layers. In the case of sample A a three-layer model was necessary to describe the data after annealing [see Fig. 3(a)]. As concluded from the obtained dispersion δ, the first layer on top of the substrate is a thin nickel oxide layer, while the second layer is an 8.2-nm-thick nickel ferrite film [48]. The third layer on top of the nickel ferrite film consists of an oxide layer with a diluted dispersion δ and thus a reduced electron density. Taking into account the NiO formation on top of sample A seen in the soft XPS spectra, we can attribute the upper layer to NiO segregation to the surface. The low electron density of this layer indicates a deconstructed film or island formation on the surface.

For sample B, however, the XRR is modeled with a single homogeneous 7.1-nm-thick nickel ferrite film on top of the substrate [see Fig. 3(b)]. For both samples the thicknesses of the residual films almost coincide with the sum of the initial thicknesses of the Fe_3O_4 and NiO films.

The slight increase in the overall thickness can be attributed to a volume increase of ∼8% due to the formation of nickel ferrite.

TABLE I. Model parameters used for the XRR intensity calculations, with dispersion δ, surface roughness σ, and film thickness d.

	Substrate		Layer 1			Layer 2			Layer 3		
	δ	σ (Å)	δ	σ (Å)	d (nm)	δ	σ (Å)	d (nm)	δ	σ (Å)	d (nm)
Sample A											
As prepared[a]	1.48×10^{-4}	2.4	2.15×10^{-4}	1.7	5.6	1.65×10^{-4}	3.9	5.5			
Annealed[b]	1.50×10^{-5}	0.1	1.7×10^{-5}	6.0	1.4	1.58×10^{-5}	2.0	8.2	1.34×10^{-5}	3.0	1.9
Sample B											
As prepared[a]	1.48×10^{-4}	2.7	2.15×10^{-4}	1.9	1.5	1.65×10^{-4}	3.2	5.5			
Annealed[b]	1.50×10^{-5}	0.1	1.58×10^{-5}	1.0	7.1						

[a]Measured at a photon energy of 2500 eV.
[b]Measured at a photon energy of 8048 eV.

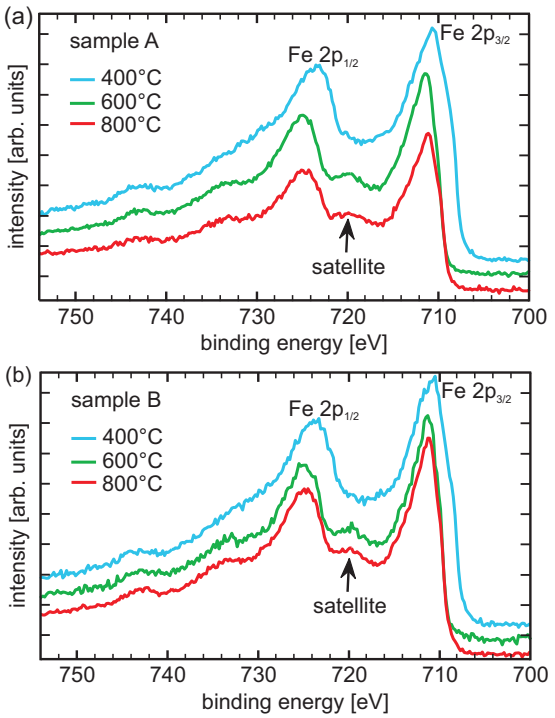

FIG. 4. HAXPES spectra of Fe $2p$ core level at 10° off-normal photoelectron emission after annealing at different temperatures (a) for sample A and (b) for sample B.

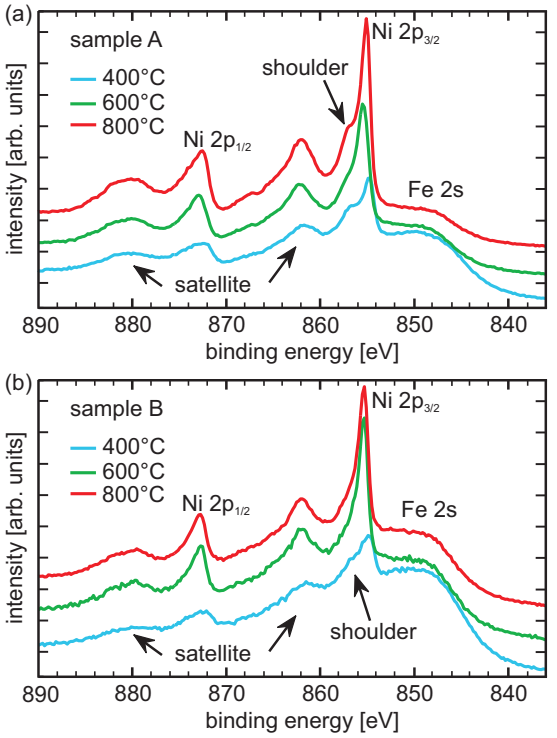

FIG. 5. HAXPES spectra of Ni $2p$ core level at 10° off-normal photoelectron emission after annealing at different temperatures (a) for sample A and (b) for sample B.

C. HAXPES

In contrast to soft x-ray photoemission, HAXPES measurements allow us to identify the valence states and chemical properties not only at the near-surface region but with bulk sensitivity due to higher excitation energy and thus increased information depth.

Figure 4 shows the HAXPES spectra for the Fe $2p$ core level, which is split into the Fe $2p_{1/2}$ and Fe $2p_{3/2}$ peaks (see soft XPS spectra, Fig. 2). Spectra recorded after each annealing step for both samples are presented. The shape of the spectra is determined by the relative fraction of Fe valence states, which is used to identify the material composition [40]. After the initial annealing step at 400 °C, there is no satellite peak visible between the two main peaks, indicating stoichiometric Fe_3O_4 for both samples. After the second and third annealing steps, at 600 °C and 800 °C, respectively, a satellite peak becomes visible between the two main peaks for both samples. As it resides on the side of the Fe $2p_{1/2}$ peak, it indicates a deficiency of Fe^{2+} ions in favor of Fe^{3+} ions compared to the initial magnetite stoichiometry. In addition, similar to the XPS results, an energy shift to higher binding energies can be seen after the second and third annealing steps, pointing to the formation of trivalent Fe^{3+} [40–42]. Thus, this behavior is in accordance with the results obtained from soft XPS spectra.

Figure 5 shows the photoelectron spectra for the Ni $2p_{1/2}$ and Ni $2p_{3/2}$ core level of both samples. After the annealing step at 400 °C the main Ni $2p_{3/2}$ peak is located at a binding energy of 854.5 (±0.2) eV, indicating NiO stoichiometry [43]. Further, for both samples, a shoulder on the high-binding-energy side of the Ni $2p_{3/2}$ peak is visible, which is also typical for NiO [43,47]. This shoulder almost completely disappears after annealing at 600 °C for both samples. Biesinger *et al.* [49] identified such a peak shape without a shoulder for the spinel-type material $NiFe_2O_4$. In addition, the Ni $2p_{3/2}$ peak is shifted to a higher binding energy of 855.0 (±0.2) eV, which is comparable to binding energy reported for Ni in $NiFe_2O_4$ stoichiometry [43]. The small mismatch between the measured value and the literature is due to an overlap of intensities originating from several layers with slightly different stoichiometries. In summary, similar to the soft XPS results, an exchange of Fe^{2+} ions with Ni^{2+} ions in the Fe_3O_4 spinel structure through interdiffusion seems to be likely [50].

For sample B, the peak shape does not change with the next annealing step at 800 °C [see Fig. 5(b)]. However, for sample A the shoulder on the high-binding-energy side re-appears, as observed for the initial bilayer system [see Fig. 5(a)]. Additionally, the Ni $2p_{3/2}$ peak is shifted to a lower binding energy, suggesting the formation of NiO-like structures, which is consistent with the NiO formation at the surface seen in the XRR and soft XPS measurements.

Furthermore, a quantitative analysis of the photoelectron spectra was performed to prove the formation of nickel ferrite. After subtracting a Shirley background, the intensities I_{Fe} and I_{Ni} of the Fe $2p$ peaks and the Ni $2p_{1/2}$ peak (due to the overlap with the Fe $2s$ peak, the Ni $2p_{3/2}$ peak has not been considered) have been numerically integrated. From these results, the relative photoelectron yield

$$Y_{Ni} = \frac{I_{Ni}/\sigma_{Ni}}{I_{Ni}/\sigma_{Ni} + I_{Fe}/\sigma_{Fe}} = \frac{N_{Ni}}{N_{Ni} + N_{Fe}C(\varphi)} \qquad (2)$$

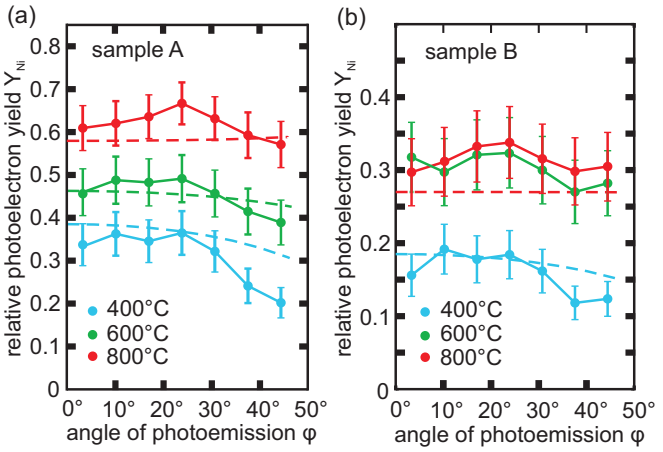

FIG. 6. Relative photoelectron yield at different off-normal emission angles (a) for sample A and (b) for sample B. The dashed lines show the calculated intensities using the models obtained from XRR analysis.

of Ni has been calculated, using the differential photoionization cross sections σ reported by Trzhaskovskaya *et al.* [51]. Newberg *et al.* [52] derived that this yield is equal to the atomic ratios but modified with a factor $C(\varphi)$ that depends on the angle of photoemission (neglecting photoelectron diffraction effects). The resulting yields from different detection angles are plotted in Fig. 6. The curves from the data of the first annealing steps show for both samples a decreasing yield for higher emission angles, as indicated by the blue dashed lines. This behavior points to an intact stack of oxide films due to a longer pathway of the photoelectrons for higher emission angles. The lines are calculated for a stack of two separated Fe_3O_4/NiO films using the thicknesses obtained from XRR analysis. With the successive annealing steps, the photoelectron yield from Ni increases, which indicates that there is diffusion of Ni into the Fe_3O_4 film and/or Fe into the NiO film.

Since there is no evidence of NiO in the Ni $2p$ HAXPES spectra after annealing at 600 °C, a model consisting of a stoichiometric 8.2-nm-thick $NiFe_2O_4$ on top of a 3.4-nm-thick NiO layer was used for sample A [green dashed line Fig. 6(a)].

With further annealing at 800 °C the intensity ratios [Fig. 6(a)] show a continuous increase of the nickel intensity. This indicates that more Ni atoms are diffusing/transported through the nickel ferrite layer to the very surface forming NiO as detected by XRR and soft XPS measurements. The photoelectron yield for this annealing step (dashed red line) was calculated using the layer structure and thicknesses obtained from the XRR analysis [see inset in Fig. 3(a)]. This model is based on a stoichiometric 8.2-nm-thick $Ni_xFe_{3-x}O_4$ film with $x = 1$ between two NiO films. The supposed segregation behavior of Ni and the formation of NiO at the surface could be explained by its lower surface energy of 0.863 J/m^2 compared to the surface energy of 1.235 J/m^2 for $NiFe_2O_4$(001) [53]. Thus, one would expect an inversion of the initial bilayer ordering with NiO under magnetite. However, during the diffusion process Ni is partly incorporated in the initial magnetite film, and stoichiometric $NiFe_2O_4$ is formed. After saturation of the nickel ferrite the residual Ni starts to form NiO at the surface. In our case, however, this process is obviously not completed due to kinetic effects, and residual NiO is still underneath the nickel ferrite.

In the case of sample B one can conclude that a single homogeneous film was already formed by the interdiffusion process after the second annealing step. Its stoichiometry does not change from the second to the third annealing step [see Fig. 6(b)]. The ratio of Ni and Fe, assuming a complete intermixing, can be determined from Eq. (2), as then the angular factor $C(\varphi) \equiv 1$. The amount of nickel and iron does not match the ratio of 1:2 for stoichiometric nickel ferrite and is 1:2.6 for sample B, indicating an excess of Fe atoms. The experimental data are in good agreement with the calculated behavior (dashed red line) for a homogeneously mixed single layer, which is also consistent with the model obtained from XRR. Thus, the resulting stoichiometry of sample B is $Ni_xFe_{3-x}O_4$, with $x = 0.83$.

The simulation of the photoelectron yield does not describe the measured data in full detail but gives an idea of the possible course. One limitation is that a model consisting of a stack of separated homogeneous layers was used. Thus, potential concentration gradients or clusters are not implemented in the simulation. Further, effects caused by x-ray photoelectron diffraction (XPD) are not considered. Nevertheless, the general trend is described well.

D. SR-XRD

Figure 7 shows SR-XRD measurements and calculated CTR intensity along the (00L) direction close to the perovskite $SrTiO_3(002)_P$ and spinel $(004)_S$ Bragg peaks for both samples after annealing. Here, L denotes the vertical scattering vector in reciprocal lattice units (r.l.u.) with respect to the lattice constant of the $SrTiO_3$(001) substrate. Indices P and S indicate

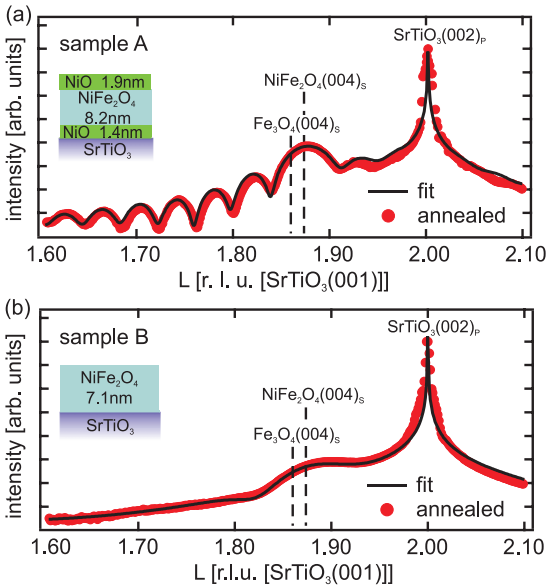

FIG. 7. SR-XRD measurements along the (00L) direction and calculated intensities. The insets show the layer structures used in the calculation. The model is similar to that obtained from the analysis of the XRR (see inset in Fig. 3).

the bulk notation for perovskite-type and spinel-type unit cells, respectively.

For both samples a clear peak from the $SrTiO_3(001)$ substrate at $L = 2$ and a broad Bragg peak originating from the oxide film around L $\approx$ 1.87 is observed. The structural parameters, e.g., vertical layer distances, are determined by analyzing the CTRs by applying full kinematic diffraction theory. The structural models obtained from the XRD analysis coincide with the layer models used for the XRR calculations of the annealed samples (see insets of Figs. 7 and 3).

For sample A the model consists of a $NiFe_2O_4$ layer between two thin NiO films (see inset in Fig. 7). The distinct oscillations close to the Bragg peak of the oxide film (Laue fringes) can be clearly attributed to the nickel ferrite layer, indicating a well-ordered homogeneous film of high crystalline quality. The diffracted intensity originating from the NiO results in a broad peak underneath the Bragg reflection of the nickel ferrite due to the small film thicknesses of the NiO films which cannot directly be seen by the bare eye in the experimental data. Furthermore, the vertical lattice constants obtained from curve fitting are $c_{\mathrm{NiO}} = 0.4177$ nm for the NiO films and $c_{NFO} = 0.8334$ nm for the $NiFe_2O_4$ layer. These results are in good agreement with the bulk values of $a^{\mathrm{bulk}}_{\mathrm{NiO}} = 0.4176$ nm and $a^{\mathrm{bulk}}_{NFO} = 0.8339$ nm, respectively.

For sample B the Laue oscillations completely vanish, pointing to inhomogeneities within the film [see Fig. 7(b)]. This effect is possibly caused by the excess of Fe atoms in the film, as observed by HAXPES. However, the peak width is in accordance with the $NiFe_2O_4$ thickness of 7.1 nm. In addition, the vertical lattice constant $c_{NFO} = 0.8304$ nm obtained from the calculations confirms the presence of a strongly distorted structure of the annealed film since it is notably lower than the value of bulk $NiFe_2O_4$.

E. XMCD

XMCD has been employed after the overall annealing cycle to analyze the resulting magnetic properties element specifically after annealing at 800 °C. Figure 8 depicts the XMCD spectra of samples A and B performed at the Fe $L_{2,3}$ and Ni $L_{2,3}$ edges, respectively. Both samples show a strong Ni dichroic signal [see Fig. 7(a)], and in order to extract the spin magnetic moments we use the spin sum rule developed by Chen *et al.* [54]. The number of holes is determined from the charge-transfer multiplet simulations for each sample. We also account for the core-hole interactions which mix the character of the L_3 and L_2 edges [55,56] by considering the spin sum rule correction factors obtained by Teramura *et al.* [55]. We find a Ni spin moment of 0.51 μ_B/Ni atom and an orbital contribution of 0.053μ_B/Ni atom, summing up to a total Ni moment of 0.56μ_B for sample A. In the case of sample B we derive $m_{\mathrm{spin}} = 0.91\mu_B$/Ni atom, $m_{\mathrm{orb}} = 0.122\mu_B$/Ni atom, and hence a total Ni moment of 1.03 μ_B/f.u.. The latter value is rather close to that recently found by Klewe *et al.* [57] on a stoichiometric $NiFe_2O_4$ thin film.

Turning to the Fe moments, we find strong indications that our heat and diffusion experiments lead to a $Ni_xFe_{3-x}O_4$ layer or cluster formation in both samples. Since we obtain $m_{\mathrm{spin}} = -0.028\mu_B$ $(+0.11\mu_B)$/Fe atom and $m_{\mathrm{orb}} = +0.015\mu_B$ $(+0.007\mu_B)$/Fe atom at the Fe sites of

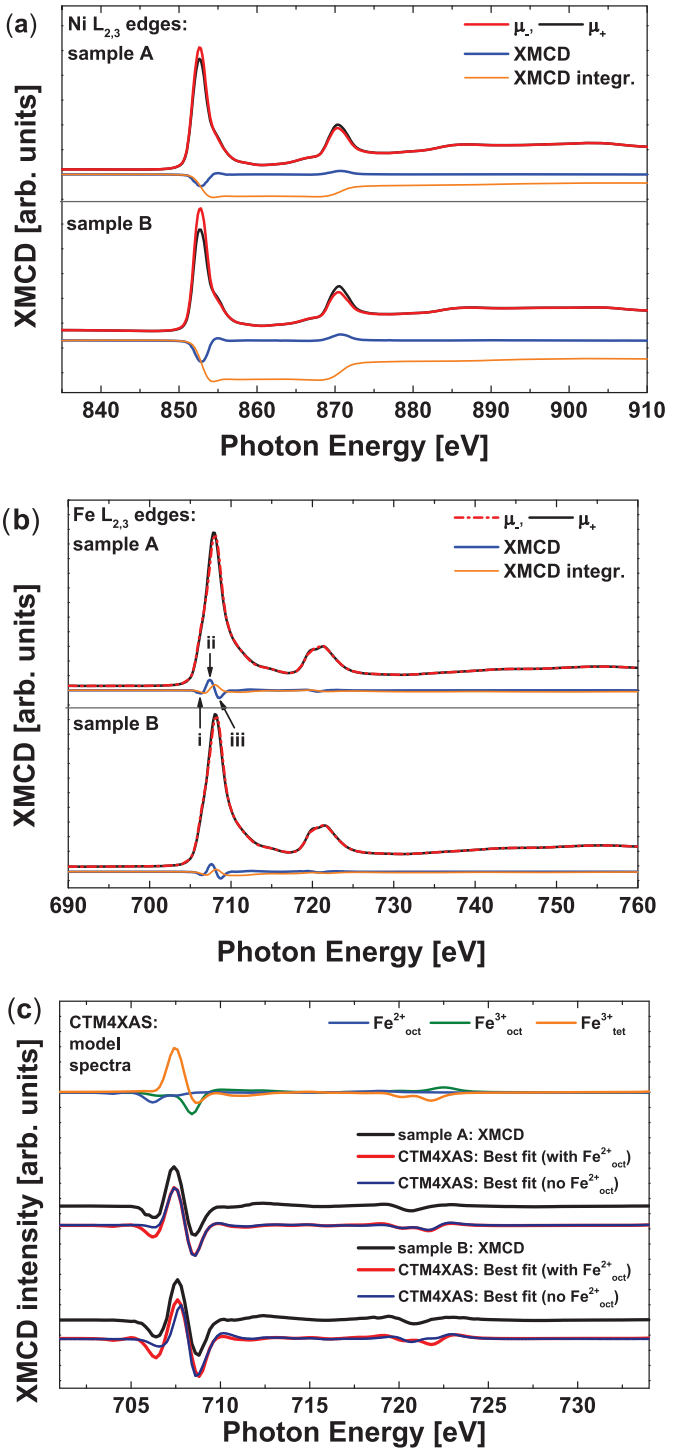

FIG. 8. (a) Ni $L_{2,3}$-XMCD spectra of samples A and B. (b) Fe $L_{2,3}$-XMCD spectra of samples A and B. (c) Experimental Fe $L_{2,3}$ edge XMCD of samples A and B and the corresponding XTM4XAS fits with and without considering octahedral coordinated Fe^{2+} ions.

sample A (sample B), we find very small net contributions to the overall magnetic moments. In comparison Klewe *et al.* [57] found an iron spin moment of around 0.1μ_B/Fe atom and a further orbital contribution of around 10%–15% of that value. This indicates an (almost complete) structural inversion of the prior bilayer system; that is, the iron ions occupy in equal parts

octahedral and tetrahedral positions within the crystal. Since the moments of these octahedrally and tetrahedrally coordinated cations are aligned antiparallel, the moments nearly cancel each other out in a perfect inverse spinel structure.

Figure 8(c) presents the charge-transfer multiplet calculations for the single iron cations in octahedral and tetrahedral coordination as well as the best fits to the experimental Fe $L_{2,3}$-XMCD spectra of samples A and B with (red) and without (blue) considering Fe^{2+}_{oct} ions. The resulting lattice site occupancies are 16.3% Fe^{2+}_{oct}, 32.2% Fe^{3+}_{oct}, and 51.5% Fe^{3+}_{tet} (42.6% Fe^{3+}_{oct} and 57.4% Fe^{3+}_{tet}) for sample A and 24.0% Fe^{2+}_{oct}, 31.5% Fe^{3+}_{oct}, and 44.5% Fe^{3+}_{tet} (55.6% Fe^{3+}_{oct} and 44.4% Fe^{3+}_{tet}) for sample B when including (not including) Fe^{2+}_{oct} ions in the respective fit. The result that, for sample A, over 50% are in Fe^{3+}_{tet} coordination as to the calculations also corresponds to the small negative spin moment determined by the spin sum rule.

From the overall multiplet fits [Fig. 8(c)] one can clearly see that feature *i* [Fig. 8(b)] is very small if Fe^{2+}_{oct} cations are not explicitly considered in the respective simulations. The origin of this feature in ferrites with inverse spinel structure other than magnetite is still not entirely understood [44,57,58]. In Fe $L_{2,3}$-XMCD spectra of both samples A and B peak *i* is significantly smaller than results obtained very recently for $NiFe_2O_4$ thin films grown by pulsed laser deposition (PLD) [44] but somewhat more intense than it is in the result of Klewe *et al.* [57]. Also, their corresponding multiplet simulation resembles our approach (not considering the Fe^{2+}_{oct} sites) rather well. The presence of peak *i* in the Fe $L_{2,3}$-XMCD of sample B can at least partly be explained by the lack of Ni^{2+}_{oct} ions as to the HAXPES measurements. Since peak *i* also occurs in XMCD experiments on bulk material [58], one can think about several additional reasons for the presence of some Fe^{2+}_{oct} ions. For instance, a small fraction of the Ni ions might be present in the form of Ni^{3+} or coordinated on tetrahedral sites as a result of the interdiffusion process. Despite the fact that Ni^{2+} prefers octahedral coordination, even measurements on $NiFe_2O_4$ bulk crystals indicate that a few of the Ni ions are on tetrahedral sites [58]. Furthermore, oxidation or reduction of a fraction of the Fe at the very surface of the thin films cannot be entirely excluded as the probing depth of the total electron yield is only around 2 nm at the Fe $L_{2,3}$ and Ni $L_{2,3}$ resonances of oxides [58,59].

For sample B we also recorded element-specific hysteresis loops at the Ni L_3 edge and the site-specific loops at Fe L_3 resonances for peaks i–iii [see Fig. 8(b)]. Figure 9 displays the resulting magnetization loops. One can see the ferrimagnetic ordering between the Fe^{3+}_{tet} cations and the other Fe and Ni cations. For all octahedrally coordinated cations we probe in-plane open magnetization curves, whereas the Fe^{3+}_{tet} cations exhibit a closed, paramagnetic magnetization curve. In the out-of-plane configuration we only probed the Ni sites (see insets in Fig. 9). Whereas recently reported values of the coercive field are on the order of $H_c = 0.1$ T or more for $NiFe_2O_4$ thin films [44,57,60], we find significantly lower values for hysteresis loops of the octahedrally coordinated cations [see Fig. 9(b)], although it is difficult to obtain exact values for H_c as the magnetization curves are pretty flat. We want to point out rather flat magnetization curves appear to be typical also for $NiFe_2O_4$ epitaxial thin films [61] and

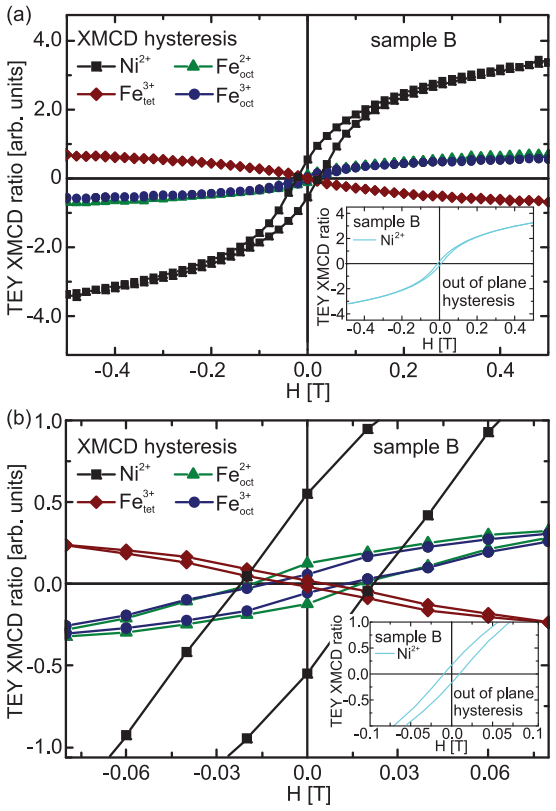

FIG. 9. (a) Element- and site-specific hysteresis loops of the Ni L_3 and Fe L_3 intensities of sample B. (b) Expanded view of the loops near $H = 0$ T. Insets show the Ni hysteresis loop measured in perpendicular (out-of-plane) geometry.

nanoparticles [62]. A number of things might be responsible for the observed discrepancy; a strongly increased H_c might be caused by exchange-coupled grains [60] or a high defect density [57], for instance. On the other hand, similar values for the coercive field measured here have been found for polycrystalline as well as epitaxial $Ni_xFe_{3-x}O_4$ thin films [61]. The bulk value of $NiFe_2O_4$ has been reported to be 0.01 T [62], which is closer to the values obtained here.

IV. SUMMARY AND CONCLUSIONS

We investigated the modification of the crystallographic, electronic, and magnetic properties of Fe_3O_4/NiO bilayers due to thermally induced interdiffusion of Ni ions out of the NiO layer into the magnetite film. We annealed two bilayers [sample A (B) initially comprises 5.6 nm (1.5 nm) NiO and 5.5 nm (5.4 nm) Fe_3O_4] in three steps of 20–30 min in an oxygen atmosphere of 5×10^{-6} mbar. LEED demonstrated the extinction of the magnetite-specific $(\sqrt{2}\times\sqrt{2})$R45° superstructure; however, a spinel-like (1×1) surface structure occurred after the overall annealing cycle.

Structural analysis reveals that the annealing cycles lead to homogeneous layers of $Ni_xFe_{3-x}O_4$. In the case of sample A consideration of an additional NiO layer on the surface and interface leads to the best agreement between calculated and experimentally observed XRR and SR-XRD results. For sample B SR-XRD indicates a strongly distorted structure

with a vertical lattice constant of $c = 0.8304$ nm, whereas the vertical lattice constant $c = 0.8334$ nm of sample A is close to that of bulk $NiFe_2O_4$ ($a_{NFO}^{bulk} = 0.8339$ nm).

These findings are supported by the soft XPS and HAXPES experiments. First, the formation of Fe^{3+} upon annealing at 600 °C is confirmed by the shape and binding energy positions of the Fe $2p$ core level spectra. Further annealing at 800 °C does not cause any changes in the Fe $2p$ spectra. Second, for sample B the shape and binding energy of the Ni $2p$ spectra indicate the formation of an inverse spinel ferrite, whereas in the case of sample A NiO characteristic features first diminish after annealing at 600 °C and then reappear after the entire annealing cycle at 800 °C. Due to surface sensitivity soft XPS analysis clearly reveals the occurrence of Ni^{2+} in NiO stoichiometry in the near-surface region after the last annealing step. Further, HAXPES analysis shows also an increasing amount of Ni^{2+} ions. This may be associated with the much thicker initial NiO layer of sample A, leading to Ni diffusion to the sample surface. We assume that $NiFe_2O_4$ is formed on top of the residual NiO film after the annealing step of 600 °C, as observed in the soft XPS and HAXPES. However, further annealing at 800 °C results in segregation and formation of NiO on top of a well-ordered stoichiometric $NiFe_2O_4$ of high crystalline quality. Thus, the nickel ferrite is saturated by Ni if the ferrite assumes $NiFe_2O_4$ stoichiometry. The residual Ni attempts to form NiO on top of the nickel ferrite due to its lower surface energy compared to the surface energy of nickel ferrite [53]. This process, however, is not completed in our case, probably due to kinetic effects.

Furthermore, we determined a Ni:Fe ratio of 1:2.6 for sample B and thus a resulting stoichiometry of $Ni_{0.83}Fe_{2.17}O_4$. This is in accordance with the weak crystalline quality of sample B seen in the XRD measurements.

We employed XMCD to study the internal magnetic properties of the thin films resulting from the Ni interdiffusion process. In excellent agreement with complementary charge-transfer multiplet simulations, we found a strong increase of the Fe_{tet}^{3+} coordinated cation fraction (around 50%) compared to stoichiometric Fe_3O_4, resulting in very small Fe net magnetic moments as determined from the experimental XMCD data by applying the sum rules. The magnetic properties after the annealing cycle are in both samples dominated by the contribution of the Ni^{2+} ions, which exhibit magnetic moments of $0.56\mu_B$/f.u. (sample A) and $1.03\mu_B$/f.u. (sample B). The latter value corresponds quite well to the value very recently reported for a stoichiometric $NiFe_2O_4$ thin film [57]. The lower value found for sample A can be explained by the formation of (antiferromagnetic) NiO-rich islands or clusters at the surface of the sample which contribute to the Ni $L_{2,3}$-XAS signal but not to the corresponding XMCD. Finally, element-specific hysteresis loops performed on sample B show a rather small in-plane coercive field. This is a further indication of the formation of a magnetically well ordered $NiFe_2O_4$-like thin film by means of thermal interdiffusion of Ni^{2+} ions into magnetite from Fe_3O_4/NiO bilayers.

In conclusion we presented a comprehensive study of epitaxially grown Fe_3O_4/NiO heterostructures and their structural evolution due to Ni interdiffusion as a consequence of three distinct thermal annealing steps. A multitechnique approach tackling the structural, chemical, electronic, and magnetic properties leads to a rather complete and conclusive picture which is also in good agreement with corresponding model calculations. We have demonstrated that it is possible to synthesize $Ni_xFe_{3-x}O_4$ thin films with compositions close to stoichiometric $NiFe_2O_4$ with high crystalline quality by thermally induced intermixing of distinct Fe_3O_4/NiO bilayers grown on Nb-doped $SrTiO_3$(001). If the initial Fe_3O_4 and NiO thin-film thicknesses can be controlled precisely, one may obtain $Ni_xFe_{3-x}O_4$ thin films with tunable band gap employing this approach, which might be of interest for several applications, e.g., in the field of spintronics (spin valves) or for experiments concerning the spin Hall magnetoresistance [29] and the spin Seebeck effect [27,28]. Thus, additional transport effects based on either charge or spin currents can be amplified or suppressed depending on the band gap properties of the $NiFe_2O_4$-like material.

ACKNOWLEDGMENTS

Financial support from the Deutsche Forschungsgemeinschaft (DFG; KU2321/2-1 and KU3271/1-1) is gratefully acknowledged. We thank Diamond Light Source for access to beamline I09 (SI10511-1) that contributed to the results presented here. Additionally, parts of this research were carried out at the light source PETRA III at DESY. We would like to thank F. Bertram for assistance using beamline P08. Furthermore, part of this work was performed at the Advanced Light Source, which is supported by the Director, Office of Science, Office of Basic Energy Sciences, of the U.S. Department of Energy under Contract No. DE-AC03-76SF00098.

[1] P. Weiss and R. Forrer, Ann. Phys. (Paris) **12**, 279 (1929).
[2] P.I. Slick, in *Handbook of Ferromagnetic Materials*, Chapter 3: Ferrites for non-microwave applications (Elsevier, Amsterdam, 1980), Vol. 2, pp. 189–241.
[3] M. I. Katsnelson, V. Y. Irkhin, L. Chioncel, A. I. Lichtenstein, and R. A. de Groot, Rev. Mod. Phys. **80**, 315 (2008).
[4] R. Bliem, E. McDermott, P. Ferstl, M. Setvin, O. Gamba, J. Pavelec, M. A. Schneider, M. Schmid, U. Diebold, P. Blaha, L. Hammer, and G. S. Parkinson, Science **346**, 1215 (2014).
[5] J. M. Byrne, N. Klueglein, C. Pearce, K. M. Rosso, E. Appel, and A. Kappler, Science **347**, 1473 (2015).
[6] K. Balakrishnan, S. K. Arora, and I. V. Shvets, J. Phys.: Condens. Matter **16**, 5387 (2004).
[7] G. E. Sterbinsky, J. Cheng, P. T. Chiu, B. W. Wessels, and D. J. Keavney, J. Vac. Sci. Technol. B **25**, 1389 (2007).
[8] F. Bertram, C. Deiter, O. Hoefert, T. Schemme, F. Timmer, M. Suendorf, B. Zimmermann, and J. Wollschläger, J. Phys. D **45**, 395302 (2012).
[9] F. Bertram, C. Deiter, T. Schemme, S. Jentsch, and J. Wollschläger, J. Appl. Phys. **113**, 184103 (2013).
[10] J. A. Moyer, S. Lee, P. Schiffer, and L. W. Martin, Phys. Rev. B **91**, 064413 (2015).

[11] T. Schemme, N. Pathé, G. Niu, F. Bertram, T. Kuschel, K. Kuepper, and J. Wollschläger, Mat. Res. Exp. **2**, 016101 (2015).
[12] N.-T. H. Kim-Ngan, A. G. Balogh, J. D. Meyer, J. Brötz, M. Zając, T. Ślęzak, and J. Korecki, Surf. Sci. **603**, 1175 (2009).
[13] K. A. Shaw, E. Lochner, and D. M. Lind, J. Appl. Phys. **87**, 1727 (2000).
[14] N.-T. H. Kim-Ngan, A. G. Balogh, J. D. Meyer, J. Brötz, S. Hummelt, M. Zając, T. Ślęzak, and J. Korecki, Surf. Sci. **602**, 2358 (2008).
[15] J. F. Anderson, M. Kuhn, U. Diebold, K. Shaw, P. Stoyanov, and D. Lind, Phys. Rev. B **56**, 9902 (1997).
[16] L. A. Kalev, P. Schurer, and L. Niesen, Phys. Rev. B **68**, 165407 (2003).
[17] H. C. Wu, R. Ramos, R. S. G. Sofin, Z. M. Liao, M. Abid, and I. V. Shvets, Appl. Phys. Lett. **101**, 052402 (2012).
[18] L. Marnitz, K. Rott, S. Niehörster, C. Klewe, D. Meier, S. Fabretti, M. Witziok, A. Krampf, O. Kuschel, T. Schemme, K. Kuepper, J. Wollschläger, A. Thomas, G. Reiss, and T. Kuschel, AIP Adv. **5**, 047103 (2015).
[19] T. Schemme, A. Krampf, F. Bertram, T. Kuschel, K. Kuepper, and J. Wollschläger, J. Appl. Phys. **118**, 113904 (2015).
[20] C. Gatel, E. Snoeck, V. Serin, and A. R. Fert, Eur. Phys. J. B **45**, 157 (2005).
[21] J. Keller, P. Miltényi, B. Beschoten, G. Güntherodt, U. Nowak, and K. D. Usadel, Phys. Rev. B **66**, 014431 (2002).
[22] T. Schemme, O. Kuschel, F. Bertram, K. Kuepper, and J. Wollschläger, Thin Solid Films **589**, 526 (2015).
[23] M. Monti, M. Sanz, M. Oujja, E. Rebollar, M. Castillejo, F. J. Pedrosa, A. Bollero, J. Camarero, J. L. F. Cuñado, N. M. Nemes, F. J. Mompean, M. Garcia-Hernández, S. Nie, K. F. McCarty, A. T. N'Diaye, G. Chen, A. K. Schmid, J. F. Marco, and J. de la Figuera, J. Appl. Phys. **114**, 223902 (2013).
[24] J. Rubio-Zuazo, L. Onandia, E. Salas-Colera, A. Munoz-Noval, and G. R. Castro, J. Phys. Chem. C **119**, 1108 (2015).
[25] M. Pilard, O. Ersen, S. Cherifi, B. Carvello, L. Roiban, B. Muller, F. Scheurer, L. Ranno, and C. Boeglin, Phys. Rev. B **76**, 214436 (2007).
[26] J.-B. Moussy, J. Phys. D **46**, 143001 (2013).
[27] D. Meier, T. Kuschel, L. Shen, A. Gupta, T. Kikkawa, K. Uchida, E. Saitoh, J.-M. Schmalhorst, and G. Reiss, Phys. Rev. B **87**, 054421 (2013).
[28] D. Meier, D. Reinhardt, M. van Straaten, C. Klewe, M. Althammer, M. Schreier, S. T. B. Goennenwein, A. Gupta, M. Schmid, C. H. Back, J.-M. Schmalhorst, T. Kuschel, and G. Reiss, Nat. Commun. **6**, 8211 (2015).
[29] M. Althammer *et al.*, Phys. Rev. B **87**, 224401 (2013).
[30] D. Levy, A. Gilberto, and M. Dapiaggi, J. Solid State Chem. **177**, 1713 (2004).
[31] C. J. Powell and A. Jablonski, Nucl. Instrum. Methods Phys. Res., Sect. A **601**, 54 (2009).
[32] S. Tanuma, C. J. Powell, and D. R. Penn, Surf. Interface Anal. **35**, 268 (2003).
[33] L. G. Parratt, Phys. Rev. **95**, 359 (1954).
[34] L. Névot and P. Croce, Rev. Phys. Appl. **15**, 761 (1980).
[35] F. M. F. de Groot, Coord. Chem. Rev. **249**, 31 (2005).
[36] E. Stavitski and F. M. F. de Groot, Micron **41**, 687 (2010).
[37] S. A. Chambers and S. A. Joyce, Surf. Sci. **420**, 111 (1999).
[38] J. Korecki, B. Handke, N. Spiridis, T. Slezak, F. Flis-Kabulska, and J. Haber, Thin Solid Films **412**, 14 (2002).
[39] R. Pentcheva, W. Moritz, J. Rundgren, S. Frank, D. Schrupp, and M. Scheffler, Surf. Sci. **602**, 1299 (2008).
[40] T. Yamashita and P. Hayes, Appl. Surf. Sci. **254**, 2441 (2008).
[41] T. Fujii, F. M. F. de Groot, G. A. Sawatzky, F. C. Voogt, T. Himba, and K. Okada, Phys. Rev. B **59**, 3195 (1999).
[42] P. C. J. Graat and M. A. J. Somers, Appl. Surf. Sci. **100-101**, 36 (1996).
[43] N. S. McIntyre and M. G. Cook, Anal. Chem. **47**, 2208 (1975).
[44] M. Hoppe, S. Döring, M. Gorgoi, S. Cramm, and M. Müller, Phys. Rev. B **91**, 054418 (2015).
[45] L. Soriano, I. Preda, A. Gutiérrez, S. Palacín, M. Abbate, and A. Vollmer, Phys. Rev. B **75**, 233417 (2007).
[46] S. Uhlenbrock, C. Scharfschwerdtt, M. Neumannt, G. Illing, and H.-J. Freund, J. Phys.: Condens. Matter **4**, 7973 (1992).
[47] A. P. Grosvenor, M. C. Biesinger, R. S. C. Smart, and N. S. McIntyre, Surf. Sci. **600**, 1771 (2006).
[48] B. L. Henke, E. M. Gullikson, and J. C. Davis, At. Data. Nucl. Data Tables **54**, 181 (1993).
[49] M. C. Biesinger, B. P. Payne, A. P. Grosvenor, L. W. M. Lau, A. R. Gerson, and R. S. C. Smart, Appl. Surf. Sci. **257**, 2717 (2011).
[50] R. M. Cornell and U. Schwertmann, *The Iron Oxides*, 2nd ed. (Wiley-VCH, Weinheim, 2003).
[51] M. B. Trzhaskovskaya, V. I. Nefedov, and V. G. Yarzhemsky, At. Data Nucl. Data Tables **77**, 97 (2001).
[52] J. T. Newberg, D. E. Starr, S. Yamamoto, S. Kaya, T. Kendelewicz, E. R. Mysak, S. Porsgaard, M. B. Salmeron, G. E. Brown, Jr., A. Nilsson, and H. Bluhm, Surf. Sci. **605**, 89 (2011).
[53] C. J. O'Brien, Z. Rak, and D. W. Brenner, J. Phys.: Condens. Matter **25**, 445008 (2013).
[54] C. T. Chen, Y. U. Idzerda, H.-J. Lin, N. V. Smith, G. Meigs, E. Chaban, G. H. Ho, E. Pellegrin, and F. Sette, Phys. Rev. Lett. **75**, 152 (1995).
[55] Y. Teramura, A. Tanaka, and T. Jo, J. Phys. Soc. Jpn. **65**, 1053 (1996).
[56] C. Piamonteze, P. Miedema, and F. M. F. de Groot, Phys. Rev. B **80**, 184410 (2009).
[57] C. Klewe, M. Meinert, A. Boehnke, K. Kuepper, E. Arenholz, A. Gupta, J.-M. Schmalhorst, T. Kuschel, and G. Reiss, J. Appl. Phys. **115**, 123903 (2014).
[58] R. Pattrick, G. Van der Laan, C. Henderson, P. Kuiper, E. Dudzik, and D. Vaughan, Eur. J. Mineral. **14**, 1095 (2002).
[59] G. F. M. Gomes, T. E. P. Bueno, D. E. Parreiras, G. J. P. Abreu, A. de Siervo, J. C. Cezar, H.-D. Pfannes, and R. Paniago, Phys. Rev. B **90**, 134422 (2014).
[60] G. H. Jaffari, A. K. Rumaiz, J. C. Woicik, and S. I. Shah, J. Appl. Phys. **111**, 093906 (2012).
[61] C. Jin, Q. Zhang, W. B. Mi, E. Y. Jiang, and H. L. Bai, J. Phys. D **43**, 385001 (2010).
[62] A. Shan, X. Wu, J. Lu, C. Chen, and R. Wang, CrystEngComm **17**, 1603 (2015).